UC Irvine
UC Irvine Previously Published Works

Title
Shape-optimized model-based reconstruction algorithm for radiacoustic imaging

Permalink
https://escholarship.org/uc/item/4j782725

Journal
Applied Physics Letters, 128(25)

ISSN
0003-6951

Authors
Pandey, Prabodh Kumar
Gottam, Omprakash
Bjegovic, Kristina
et al.

Publication Date
2026-06-22

DOI
10.1063/5.0326437

Copyright Information
This work is made available under the terms of a Creative Commons Attribution License, available at https://creativecommons.org/licenses/by/4.0/

Peer reviewed

eScholarship.org Powered by the California Digital Library
University of California

Applied Physics Letters

RESEARCH ARTICLE | JUNE 23 2026

Shape-optimized model-based reconstruction algorithm for radiacoustic imaging

Prabodh Kumar Pandey ; Omprakash Gottam ; Kristina Bjegovic ; Gilberto Gonzalez ; Yong Chen ; Liangzhong Xiang

Check for updates

Appl. Phys. Lett. 128, 253701 (2026)
https://doi.org/10.1063/5.0326437

View Online
Export Citation

Articles You May Be Interested In

Multi-parameter assessment of osteoporosis based on x-ray induced acoustic computed tomography

Appl. Phys. Lett. (September 2025)

30 October 2026 20:07:56

Nanotechnology & Materials Science
Optics & Photonics
Impedance Analysis
Scanning Probe Microscopy
Sensors
Failure Analysis & Semiconductors

Unlock the Full Spectrum.
From DC to 8.5 GHz.

Zurich Instruments
Find out more

AIP Publishing

Applied Physics Letters ARTICLE pubs.aip.org/aip/apl

Shape-optimized model-based reconstruction algorithm for radiacoustic imaging

Cite as: Appl. Phys. Lett. **128**, 253701 (2026); doi: 10.1063/5.0326437
Submitted: 5 February 2026 · Accepted: 1 June 2026 ·
Published Online: 23 June 2026

View Online Export Citation CrossMark

Prabodh Kumar Pandey,[1,a)] Omprakash Gottam,[2] Kristina Bjegovic,[3] Gilberto Gonzalez,[4] Yong Chen,[4] and Liangzhong Xiang[1,3,5,a)]

AFFILIATIONS

[1]Department of Radiological Sciences, University of California, Irvine, California 92697, USA
[2]Department of Electronics and Communications, Koneru Lakshmaiah Education Foundation, Hyderabad 500075, Telangana, India
[3]Department of Biomedical Engineering, University of California, Irvine, California 92697, USA
[4]Department of Radiation Oncology, University of Oklahoma Health Sciences Center, Oklahoma City, Oklahoma 73104, USA
[5]Beckman Laser Institute, University of California, Irvine, Irvine, California 92612, USA

[a)]**Authors to whom correspondence should be addressed:** pkpandey@hs.uci.edu and liangzhx@hs.uci.edu

ABSTRACT

We present a shape-optimized model-based reconstruction framework that addresses the limited-view problem in radiacoustic imaging arising from restricted detector placement, which creates severely ill-posed inverse problems that manifest as characteristic artifacts in reconstructed images. We first reconstruct an approximate dose-region boundary using a parametric level set–based shape optimization. Pointwise model-based dose reconstruction is then performed only within this shape-constrained region. By restricting reconstruction from the full imaging domain to only the pixels within the identified region, the number of unknowns is significantly reduced, transforming a severely ill-posed inverse problem into a much better-constrained one. We validate this methodology through computational studies and experiments using clinical x-ray and proton radiation sources under limited angular coverage data acquisition settings. Results demonstrate substantial artifact reduction and improved accuracy compared to standard model-based reconstructions, with a 3%–25% improvement in correlation coefficients across different imaging settings, with the more pronounced improvements occurring under stronger limited-view conditions. This shape-optimized approach provides a viable pathway for accurate radiation therapy monitoring under clinically realistic detector configurations.

Published under an exclusive license by AIP Publishing. https://doi.org/10.1063/5.0326437

30 October 2026 20:07:56

Radiacoustic imaging (RAI)[1] is a fast evolving imaging technique based on radiation-based excitation and acoustic detection. Since its inception in 2013,[2] RAI has been explored by several groups for its applications in structural imaging[3–11] as well as radiation dosimetry.[12–22] The theory of RAI is that the absorption of temporally short radiation pulses in tissues generates ultrasound (US) detectable by ultrasonic transducers[2] (UTs) placed around the irradiated object. The collected US signals can then be fed to image reconstruction algorithms to reconstruct the map of dose distribution in the object. The 3D US propagation enables single-projection 3D imaging, reducing the need for rotating sources and detectors as needed by CT.[23]

RAI has found a niche application in radiation therapy (RT) monitoring. Advances in RT have made it a precise cancer treatment, but current techniques rely on pretreatment imaging[24–26] and lack *in vivo*, real-time monitoring. RAI addresses this gap and has rapidly progressed from a research tool[2,13–15,19,27–30] to early animal and patient studies,[20,22] demonstrating strong potential for clinical translation. RAI-based dosimetry can be integrated into existing RT systems with minimal modifications, enabling seamless clinical implementation.

One of the major challenges in RAI is the limited-view problem, as clinical constraints restrict detector placement to a small angular window, resulting in incomplete RA measurements. RAI reconstruction aims to recover the initial pressure distribution ($\propto$ deposited dose) from these signals. Conventional back-projection (BP)[2] and time reversal[31] methods are highly sensitive to noise and limited-view effects. Model-based (MB)[8,32] algorithms improve noise robustness but offer limited mitigation of limited-view artifacts due to the inherent ill-posedness of the inverse problem (IP). Incomplete detector coverage leads to a severely ill-conditioned system matrix,[33,34] with conditioning worsening as

Published under an exclusive license by AIP Publishing

the reconstruction region of interest (ROI) increases relative to the detector geometry.[35] Larger ROIs therefore suffer from reduced angular coverage,[36,37] amplifying measurement errors and necessitating regularization for stable reconstruction.[38]

Shape-based reconstruction frameworks are well-suited for such IPs in imaging.[39–43] These frameworks have the potential to resolve the inherent ill-posedness in IPs by assuming that the target has distinct piece-wise regions. Level-set representation is an efficient tool in shape reconstruction to reduce the dimensionality and improve the computational tractability of the IP.[42,44,45] Parametric level sets based on the linear combination of radial basis functions (RBFs) have been used to solve for the boundary of abnormal absorption coefficient in diffuse optical tomography[42,46] as well as to identify the cancerous tissue region using fluorescence-based optical and photoacoustic tomography.[44,45] The boundaries of metallic targets are imaged from backscattered electromagnetic measurements using shape optimization frameworks.[47] The accelerated level-set approach is used to reconstruct the shape of obstacles.[48] This demonstrates the potential of shape-based reconstructions for stable and accurate results. Here, we propose a two-stage shape-optimized model-based (SOMB) RAI reconstruction framework that addresses limited-view artifacts through spatial constraint. In stage-1, we reconstruct the approximate boundary of the dosed region rather than attempting to recover pixel-wise dose. This boundary is represented using parametric level sets—a mathematical representation requiring only 100 parameters instead of 10 000+ pixel values—and is optimized using a regularized trust-region algorithm to match the measured acoustic signals. The boundary thus obtained, with some tolerance, is considered as the compact support of the dose. In the second stage, pointwise MB dose reconstruction is performed within this reduced ROI. By restricting the inversion to this shape-informed ROI (80% less pixels than the full ROI), we rebalance the IP—the same measurements now constrain much fewer unknowns, transforming an underdetermined system into a well-constrained one. This dimensional reduction suppresses limited-view artifacts and improves reconstruction accuracy.

The propagation of RA waves generated due to instantaneous dose deposition is as follows:[49]

$$\frac{\partial^2 p(\vec{r},t)}{\partial t^2} - v^2\nabla^2 p(\vec{r},t) = \Gamma H(\vec{r})\frac{\partial \delta(t)}{\partial t}, \tag{1}$$

where Γ is the Gruneisen parameter,[50] v is the sound speed, and H is the radiation energy deposition (RED)—proportional to the dose deposition. The semi-analytic solution to Eq. (1) is given by

$$p(\vec{r},t) = \frac{\Gamma}{4\pi v}\frac{\partial}{\partial t}\left(\frac{1}{vt}\int_{S(\vec{r},t)} H(\vec{r}')dS'(t)\right); \quad |\vec{r}-\vec{r}'| = vt. \tag{2}$$

where $S'(\vec{r},t)$ denotes a time-dependent spherical (circular for 2D) surface centered at a detector (located at $\vec{r}$, radius vt) essentially denoting a surface of pressure sources from where the signals would be reaching the detector at time t such that $|\vec{r}-\vec{r}'| = vt$. Since this work focuses on 2D RAI, $S'(\vec{r},t)$ represents a circle instead. Dropping the constant term and further solving Eq. (2) can be further simplified as

$$p(\vec{r},t) = \frac{\partial}{\partial t}\left(\int_{S(\vec{r},t)} H(\vec{r}')d\theta\right); \quad |\vec{r}-\vec{r}'| = vt. \tag{3}$$

This can be solved by discretizing the spatiotemporal domains to obtain the acoustic measurements[8] $\underline{p}^{(q)}$ (size: $N_d \times 1$; N_d being the number of detectors) at the qth time sample due to the discrete RED map $\underline{h}$ (size: $N \times 1$; N being the number of nodes) as

$$\underline{p}^{(q)} = \mathscr{M}^{(q)}\underline{h}, \tag{4}$$

where $\mathscr{M}^{(q)}$ is the measurement operator (size: $N_d \times N$) relating the RA measurements at all the detectors at the qth time step. The contribution matrices for all the time steps can then be stacked together relating the complete acoustic measurement vector $\underline{p}$ with $\underline{h}$,

$$\underline{p} = \mathbf{M}\underline{h}, \tag{5}$$

where $\mathbf{M}$ is known as the model matrix and is stored in this work for performing image reconstruction.

The reconstruction problem in RAI is to obtain the RED map ($\underline{\hat{h}}$) from time-domain acoustic measurements ($\underline{p}_{meas}$). In MB image reconstruction algorithms, this problem is set up as a least squares minimization problem given as

$$\underline{\hat{h}} = \arg\min_{\underline{h}} ||\mathbf{M}\underline{h} - \underline{p}_{meas}||^2 + \lambda^2||\mathbf{R}\underline{h}||^2, \tag{6}$$

where $\mathbf{R}$ and λ represent a regularization matrix and regularization parameter.

In benchtop and phantom studies, RA signals can be acquired using large transducer arrays or wide-angle scanning of single transducers, enabling high-quality reconstructions. In clinical settings, however, anatomical and practical constraints limit data acquisition to narrow angular windows. Such limited-view geometries lead to severely ill-posed IPs and characteristic artifacts, including tail-like structures and missing features perpendicular to the detector array. ROI reduction using prior information is an effective strategy to mitigate this ill-posedness by restricting the reconstruction domain, thereby reducing the number of unknowns constrained by the same measurements. This acts as implicit spatial regularization, concentrating information density and shrinking the solution space, and is particularly valuable for clinical RAI where detector placement is inherently limited.

In Fig. 1, we depict a basic demonstration where we have a circular source [radius: 2 cm, Fig. 1(a)] with unit strength, and a 5 cm long 16-element linear array is placed 5 cm away from its center. The measurement RA data at these detectors are computed using a semi-analytic model.[8] The BP algorithm is then implemented for image reconstruction [Fig. 1(b)] in a 10 × 10 cm^2 domain, which carries strong artifacts due to limited-view of data collection. Being an analytic algorithm evaluated pixelwise, reconstruction in a small ROI [Fig. 1(c)] is equivalent to cropping the large ROI result. Next, an MB optimization was performed for reconstruction in the large ROI [Fig. 1(d)]. As expected, MB improves over BP but still exhibits strong limited-view artifacts and underestimates the source strength. Restricting the MB reconstruction to a smaller ROI forces the solution to explain the measured signals with a confined source. Thus, while a larger domain spreads source energy over a wider region, a smaller ROI confines it, reducing limited-view artifacts and improving quantitative accuracy [Fig. 1(e)].

To obtain an approximate ROI for RAI reconstruction, we propose employing a shape-based reconstruction that under the assumption of homogeneous source reconstructs its boundary. In shape-

30 October 2026 20:07:56

Published under an exclusive license by AIP Publishing

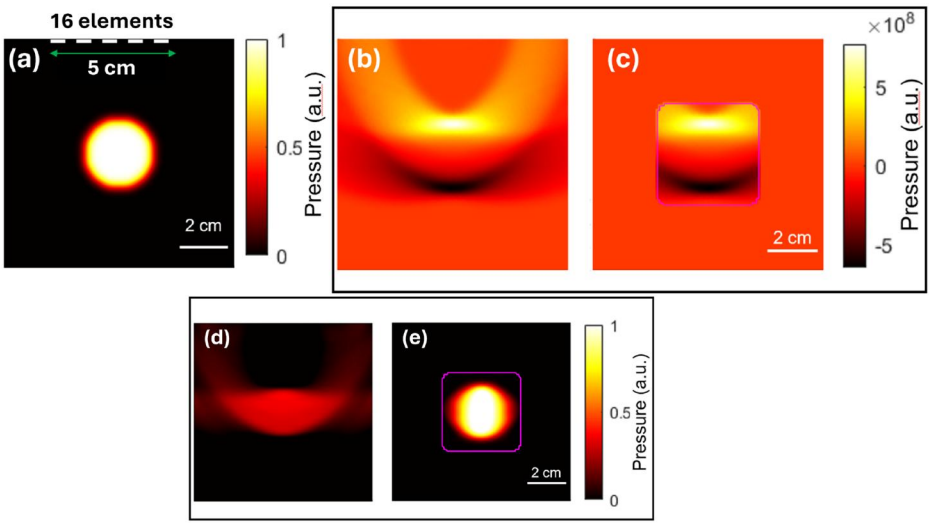

FIG. 1. Effect of ROI on BP and MB reconstruction algorithms: (a) Source-detection setup, BP reconstruction in (b) $10 \times 10\,\text{cm}^2$ and (c) $5 \times 5\,\text{cm}^2$ ROI, and MB reconstruction in (d) $10 \times 10\,\text{cm}^2$ and (e) $5 \times 5\,\text{cm}^2$ ROI.

based representation, the contrast in h can be assumed piece-wise constant and represented as[44]

$$h(\Theta) = h^i H(\phi(r,\gamma)) + h^o(1 - H(\phi(r,\gamma))), \tag{7}$$

where $H(\phi)$ is the mollified Heaviside function,[51] h^i and h^o are the values of h inside and outside. Θ is the set of parameters defining the shape (to be reconstructed): $\Theta \equiv \{ h^i, h^o, \underbrace{\alpha, \beta, \chi_1, \chi_2}_{\gamma} \}$. In this work, we have utilized the compactly supported RBF level-set.[42] More detail has been provided in supplementary material S1, and the demonstration of the formation of shapes from four such RBFs is provided in supplementary material (videos) S2–S5. For our work, we have used 24 RBFs, which we found to be good enough to reasonably represent the proton and x-ray dose map shapes.

The corresponding IP is set up as a Tikhonov-regularized least squares problem,

$$\hat{\Theta} = \arg\min_{\Theta} \mathscr{F}(\Theta) := \frac{1}{2}||(\mathbf{M}h(\Theta) - \underline{p}_{meas})||^2 + \tau||\Theta - \Theta_c||^2$$
$$= \frac{1}{2}R^T R + \tau||\Theta - \Theta_c||^2, \tag{8}$$

where τ is the regularization parameter used with the minimum-norm regularization functional, and Θ_c represents an *a priori* known constant vector. This shape optimization problem is solved using trust-region-based iteratively regularized quasi-Newton Broyden–Fletcher–Goldfarb–Shanno (BFGS) algorithm routine detailed in supplementary material S6, and the corresponding pseudoalgorithm is given in supplementary material S7 (Algorithm 1). It reconstructs the source shape by finding the set of shape parameters Θ—the centers (x, y), weights, and dilation factors for the 24 RBFs—such that the acoustic signals predicted by the forward model for the shape thus formed best fit the measured acoustic signals. The regularization term is included in the cost function in Eq. (8) to avoid overfitting to the noise. In comparison to the standard MB optimization that aims to recover ∼10 000 pixel values, this shape optimization leads to ∼100-fold dimensional reduction. The iterative shape evolution—starting from a circular initial guess and converging to the final source boundary via Algorithm 1 (supplementary material S7)—is illustrated in the upcoming figures.

Following the shape-based reconstruction, we obtain an approximate boundary of the RA pressure source defined by the optimized parameters $\hat{\Theta}$. This reconstructed shape provides an ROI that encloses the source. To account for potential boundary uncertainties, this ROI is isotropically expanded by a tolerance distance ξ in all directions to define the reduced ROI Ω_{red} for subsequent MB reconstruction,

$$\Omega_{\text{red}} = \left\{ \vec{r} \in \mathbb{R}^2 : d(\vec{r}, \partial\Omega_{\hat{\Theta}}) \leq \xi \right\}, \tag{9}$$

where $\partial\Omega_{\hat{\Theta}}$ denotes the boundary of the reconstructed shape (the zero level-set: $\{\vec{r} : \phi(\vec{r}, \hat{\gamma}) = 0\}$), and $d(\vec{r}, \partial\Omega_{\hat{\Theta}})$ represents the distance from point $\vec{r}$ to the nearest point on this boundary. The RA inverse problem is then re-solved within this reduced ROI using the MB least-squares formulation. Let $\mathscr{I}_{\text{red}} = \{i : \vec{r}_i \in \Omega_{\text{red}}\}$ denote the set of indices corresponding to nodes within Ω_{red}, and N_{red} is the number of nodes within Ω_{red}. The discrete RED map restricted to Ω_{red} is denoted as $\underline{h}_{\text{red}}$ (size: $N_{\text{red}} \times 1$), and the corresponding measurement operator $\mathbf{M}_{\text{red}}$ (size: $N_d \times N_{\text{red}}$) is obtained by extracting the columns of $\mathbf{M}$ corresponding to nodes in Ω_{red},

$$\mathbf{M}_{\text{red}} = \mathbf{M}(:, \mathscr{I}_{\text{red}}). \tag{10}$$

The reconstruction problem becomes

$$\hat{\underline{h}}_{\text{red}} = \arg\min_{\underline{h}_{\text{red}}} ||\mathbf{M}_{\text{red}}\underline{h}_{\text{red}} - \underline{p}_{\text{meas}}||^2 + \lambda^2||\mathbf{R}_{\text{red}}\underline{h}_{\text{red}}||^2. \tag{11}$$

By constraining the reconstruction domain to this smaller, shape-optimized ROI, we effectively reduce the ill-posedness of the IP, as demonstrated in Fig. 1. This two-stage approach leverages the geometric information from the shape-based method to improve the final reconstruction. The algorithms for shape-optimization and subsequent MB reconstruction algorithms are given in supplementary material S7.

To evaluate the proposed method, we conducted a computational RAI study using proton pencil beam energy deposition

30 October 2026 20:07:56

Published under an exclusive license by AIP Publishing

(107.66 MeV) in water from RayStation, a treatment planning software. A synthetic 16-element linear array (pitch 3.2 mm) was placed 3.5 cm from the Bragg peak [Fig. 2(a)]. RAI measurements were simulated using a semi-analytic model[8] at 8 MHz sampling and 0.5 mm grid resolution. White Gaussian noise was added to achieve 5 dB SNR, and the proposed algorithm was applied for reconstruction. The model matrix was first computed and stored using a 1 mm grid and 2 MHz sampling, and the measurement data were downsampled accordingly to 241 samples. This lower sampling rate reduces computational load and is adequate since RA waves from diffuse proton deposition are reported to be around hundreds of kHz.[52] The model matrix was then used to evaluate reconstructions with the proposed shape-optimized MB algorithm and compare them to standard MB reconstructions.

The proposed methodology was also validated experimentally using clinical x-ray and proton sources with RA detection via single-element scanning and array measurements. At the OU Health Science Center, a Varian TrueBeam 10 MV linac irradiated water in a tank while an Olympus single-element ultrasound probe (0.5 MHz center frequency, 100% fractional bandwidth at −6 dB) was scanned along a 130 mm circular path centered on the beam axis. RA waveforms were recorded at 60 uniform angles around the 40 × 40 mm^2 irradiation field. RAI reconstructions were evaluated within a 10 × 10 cm^2 imaging domain at the center.

The experimental proton RAI setup uses a Mevion S250i synchrocyclotron to deposit dose in water, generating proton-induced RA signals. A scintillator-photodiode assembly provided beam pulse detection and synchronization triggers. RA data were acquired using a 256-element (16 × 16) 2D ultrasonic array (Doppler Tech Inc., dimensions: 50 × 50 mm^2, nominal frequency of 1 MHz, fractional bandwidth ∼60% at −6 dB). Signals were digitized using a 256-channel Legion ADC module (Photosound Technologies) with system control hardware. The accelerator delivers proton pulses at 750 Hz with energies of 45.5–227.15 MeV, corresponding to penetration depths of ∼19–320 mm in water. The array was placed coaxially in a water tank, and trigger pulses from a Keysight 33600A waveform generator initiated acquisition of ∼75 μs RA signals across all channels. Front-end amplification provided up to 91 dB gain. For 2D reconstruction, only a single column (16 channels) was used, and the detector impulse response and proton pulse profile were deconvolved from the signals prior to reconstruction.

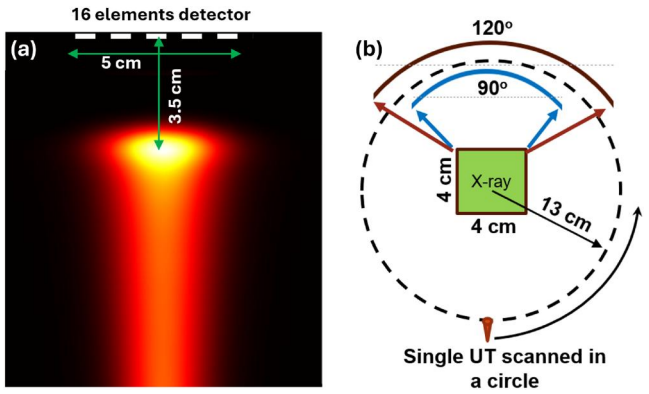

FIG. 2. Detection geometries: Detection setup for (a) proton RAI (computational + experimental) and (b) x-ray RAI also demonstrating the two limited-view scenarios considered with 120° and 90° angular coverage.

The *in silico* results are shown in Fig. 3. The standard MB reconstruction in the 10 × 10 cm^2 domain [Fig. 3(b)] locates the Bragg peak (BP) accurately compared with the true map [Fig. 3(a)], but exhibits tail-like limited-view artifacts and poor reconstruction of the pre-BP region, a known issue when structures perpendicular to the transducer array are not well sensed.[53,54] The shape reconstruction algorithm was then applied, and Fig. 3(e) shows the evolution of the reconstructed shape over 180 iterations starting from a 3 cm radius circle. The resulting shape reasonably represents the proton dose deposition and, with a 5 mm isotropic tolerance [Fig. 3(c)], we define the reduced ROI. MB optimization within this ROI [Fig. 3(d)] significantly reduces tail artifacts and recovers about 4 cm of the pre-BP region missing in the standard MB reconstruction. Reconstruction accuracy was quantified using Pearson's correlation coefficient (CC) between the reconstructed dose distribution $\hat{h}$ and ground truth h^{GT},

$$\mathrm{CC} = \frac{\sum_{i=1}^{N}(\hat{h}_i - \bar{\hat{h}})(h_i^{GT} - \bar{h}^{GT})}{\sqrt{\sum_{i=1}^{N}(\hat{h}_i - \bar{\hat{h}})^2}\sqrt{\sum_{i=1}^{N}(h_i^{GT} - \bar{h}^{GT})^2}}, \tag{12}$$

where $\bar{\hat{h}}$ and $\bar{h}^{GT}$ are the respective means of $\hat{h}$ and h^{GT}, and N is the total number of pixels in the reconstruction domain. The SOMB reconstruction yields a higher CC of 0.77 vs 0.52 from the MB. Shape reconstruction required ∼4 s, while MB reconstruction took 0.02 s for the full ROI and 0.008 s for the reduced ROI using MATLAB's "lsqr" function.

Figure 3(f) shows the singular value spectra for model matrices for the full system M [3856 (16 detectors ×241 time samples) measurements × 10 201 unknowns] and the shape-reduced system M_{red} (3856 measurements × 1795 unknowns). The effective ranks of the two systems determined by identifying the point at which the magnitudes undergo a catastrophic decay are found to be ∼2400 and 1300, respectively, indicating higher information content in the full system, as the large ROI has a greater number of independent source locations and paths for the acoustic waves to be sensed by the transducer array. However, the condition number (ratio of the maximum to minimum singular values) for the full system was found to be $\sim 4.7 \times 10^{27}$, indicating extreme ill-conditioning and numerical singularity. In contrast, the reduced ROI lowered this to $\sim 7.6 \times 10^{16}$, representing stability improvement of over ten orders of magnitude, significantly lowering the sensitivity of the IP to measurement noise. The fundamental mechanism underlying the overall improvement is dimensional reduction of the unconstrained parameter space. The shape prior reduces total unknowns by ∼80% (from 10 201 to 1795) while the effective rank reduces only from 2400 to 1300 components. As a result, the null space shrinks from ∼7800 in the full ROI to only ∼500 in the reduced ROI, thereby reducing reconstruction ambiguity and preventing null-space-related artifacts.

To study the sensitivity of the shape reconstruction w.r.t. the initial guess, five test cases were examined: in cases 1 and 2, the center of the initial guess was shifted by 1 cm in the y and x directions, respectively, while in case 3, the initial guess was a deformed circle. Cases 4 and 5 demonstrate the cases where the initial guess is significantly larger and smaller than the target of the reconstruction. Shape

30 October 2026 20:07:56

Published under an exclusive license by AIP Publishing

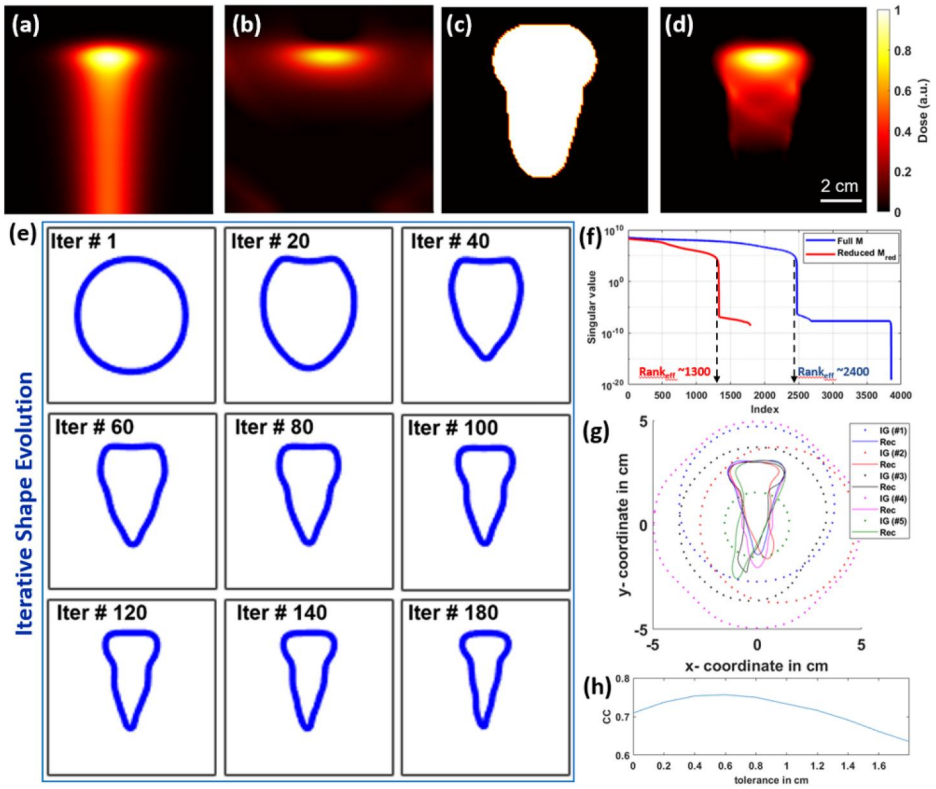

FIG. 3. Proton RAI *in silico* study result. (a) The original RA source map, (b) standard MB reconstruction (CC = 0.52), (c) the shape reconstruction obtained from algorithm 1, and (d) the MB RAI reconstruction evaluation in the reduced ROI (CC = 0.77). (e) The evolution of the reconstructed shape using algorithm 1 across iterations. (f) Singular value spectra for the full and shape-optimized reduced ROI systems with their effective ranks indicated. (g) Initial guesses (IG) for five test cases and corresponding shape reconstructions, and (h) the variation of the CC with the tolerance distance ξ [ROI: $10 \times 10\,\text{cm}^2$].

optimization was performed for all five cases, with results shown in Fig. 3(g). All test cases successfully recovered the location and shape of the region near the Bragg peak. However, the influence of the initial guess becomes evident in the reconstructed shape at locations farther from the transducer array, toward the distal tail of the Bragg peak. This is expected, as acoustic signals originating from deeper regions are both weaker in amplitude and captured with limited angular coverage by the detector array. Consequently, the final solutions exhibit greater sensitivity to the initial guess in these regions. Moreover, if the initial shape estimate is too small, the shape optimization algorithm diverges because the forward model produces a very weak source. Hence, the residual gradient has minimal useful information, and the optimizer has no meaningful descent direction.

To assess sensitivity to the tolerance distance parameter ξ, we varied the tolerance from 0 to 18 mm in 2 mm increments and performed model-based (MB) image reconstruction within the corresponding ROIs. The correlation coefficient (CC) with respect to the ground truth proton dose distribution is plotted in Fig. 3(h). For small ξ, the resulting ROI is smaller than the actual source extent. Since reconstruction is constrained within this undersized ROI, portions of the true source remain unrecovered, leading to reduced CC with the ground truth. As ξ increases, the ROI becomes sufficiently large to encompass the majority of the source volume, resulting in improved reconstruction accuracy and higher CC values. However, when the tolerance becomes excessively large, and the ROI extends well beyond the source boundaries, the reconstruction begins to exhibit limited-view artifacts. These artifacts degrade the CC. At even larger ξ, the benefits offered by the shape-informed ROI diminish entirely. The problem reverts to the ill-posed nature of standard MB reconstruction without shape guidance, and the CC degrades toward baseline levels comparable to conventional MB reconstruction. The optimal tolerance distance should be selected based on prior knowledge of the reconstruction target and informed by computational tuning. For the present study, we chose a tolerance of 5 mm, which, as indicated in Fig. 3(g), lies within the range where high CC values with GT are obtained. This value represents a favorable balance between two competing factors: ensuring the ROI is sufficiently large to capture the full extent of the dose map, while remaining compact enough to minimize spurious limited-view artifacts. The algorithm was also found to be robust w.r.t. reasonable choices of regularization parameter τ and the trust-region radius Δ. The corresponding study is demonstrated in supplementary material S8.

In the x-ray RAI experiment, the MB reconstruction using the full dataset (60 detectors over the full circle) was taken as the reference [Fig. 4(a)], and reasonably represents the $4 \times 4\,\text{cm}^2$ x-ray beam cross section in water. Limited-view reconstructions from standard MB and the proposed shape-optimized MB algorithms were compared against this reference. For the first test with 120° collection (20 consecutive transducers), the standard MB result [Fig. 4(b)] is distorted with tail artifacts, while the shape reconstruction [Fig. 4(c)] locates the source accurately, and the MB reconstruction within the reduced ROI [Fig. 4(d)] shows substantially reduced artifacts. The improvement is even more pronounced for 90° collection [15 detectors, Figs. 4(e)–4(g)]. Quantitatively, the correlation coefficient relative to the full-view reference increases by 3% and 9% for 120° and 90° collection.

30 October 2026 20:07:56

Published under an exclusive license by AIP Publishing

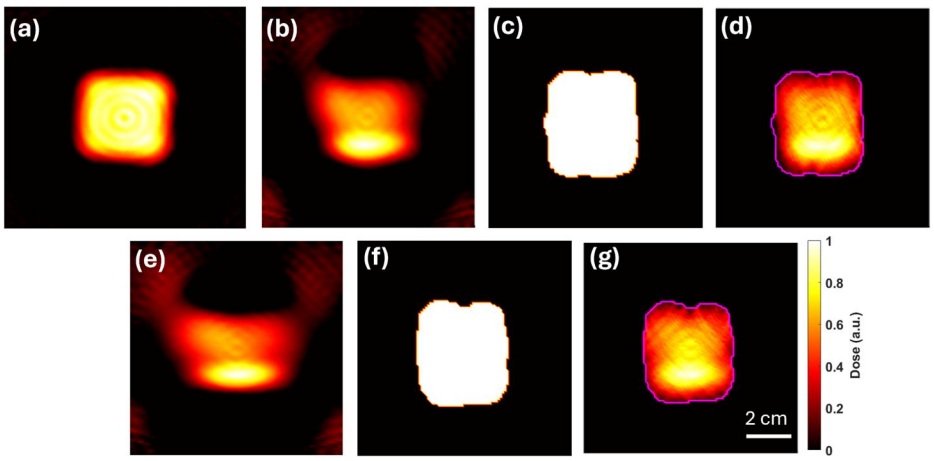

FIG. 4. X-ray RAI experimental study result. (a) MB RAI reconstruction from full (60 detectors) data (used as reference), (b) standard MB reconstruction from one-third angular coverage (20 detectors, CC = 0.90), (c) the shape reconstruction obtained from algorithm 1, and (d) the MB RAI reconstruction evaluated in the reduced ROI (CC = 0.93). (e) standard MB reconstruction from one-fourth angular coverage (15 detectors, CC = 0.84), (f) the shape reconstruction obtained from algorithm 1, and (g) the MB RAI reconstruction evaluated in the reduced ROI (CC = 0.93).

For the proton RAI experiment, the treatment plan for the delivered 107.66 MeV beam served as the reference [Fig. 3(a)]. The reference dose map is accurately known relative to the proton machine isocenter and water tank coordinate system, as beam delivery parameters are regularly verified by the clinical quality assurance program. The transducer array position relative to the water tank was measured using a ruler, yielding an estimated axial uncertainty of approximately 1 mm. Laterally, the proton beam was aligned with the transducer array center using laser-based alignment systems. All reconstructions were performed within a $10 \times 10\,\text{cm}^2$ ROI centered at 6 cm depth from the detector center, and the reference dose distribution was correspondingly extracted for quantitative comparison. The standard MB reconstruction from signals from a single line of elements [Fig. 5(a)] only recovers the BP region and shows tail artifacts, because the axial acquisition and small aperture miss most cylindrical waves from the BP tail.[52,53] Applying the shape reconstruction yields a smaller ROI [Fig. 5(b)], and the MB reconstruction within this reduced ROI reduces tail artifacts and recovers parts of the BP tail [Fig. 5(c)]. The shape evolution across iterations is shown in Fig. 5(d). Overall, the proposed shape-optimized MB strategy improves reconstruction quality, increasing the correlation coefficient by 23% from 0.36 to 0.59.

To place the proposed algorithm in the context of existing limited-view artifacts mitigation techniques, we also performed total variation (TV) regularized MB (TV-MB) reconstruction and TV-MB reconstruction with Bregman iterations (Breg+TV)[55] (TV regularization implemented through the IRtools package[56] function IRhtv), as well as prediction using a physics-informed neural network (PINN) algorithm,[57] and the results thus obtained are shown in Figs. 5(e)–5(g). In Table I, we also compared the CC and the time taken for each of these algorithms with respect to the standard MB and the SOMB reconstructions. TV-MB favors piecewise-smooth reconstructions with preserved sharp features. Compared to standard MB reconstruction (CC = 0.36), TV-MB achieves a higher CC of 0.42 and exhibits reduced tail artifacts. Breg+TV mitigates the amplitude bias inherent in TV regularization by iteratively adding the reconstruction residual back into the modified data vector. This allows the algorithm to recover signal amplitudes initially underestimated by the regularization penalty, improving accuracy without sacrificing the piecewise-smooth structure. Breg+TV further improves the correlation to CC = 0.50, with additional reduction in tail artifacts and improved capture of the Bragg peak volume. The proposed SOMB algorithm outperforms all physics-based reconstruction methods, achieving a correlation of CC = 0.59 with the ground truth while maintaining approximately 2.5-fold faster computation time compared to Breg+TV. The PINN reconstruction achieves a substantially higher CC of 0.86 by accurately recovering both the Bragg peak region and a significant portion of its tail. However, this gain comes at the cost of generalizability: data-driven methods such as PINNs are inherently setup- and geometry-specific, requiring thousands of training datasets for each configuration and necessitating retraining whenever setup changes, limiting their applicability across diverse or evolving setups.

Akin to the typical nonlinear optimization algorithms, the shape optimization method requires a reasonable initial guess and tuning of algorithm-specific parameters Δ, τ, ξ. While in the current study, this has been made based on our computational experience, we plan to perform a systematic study for automatic selection of these parameters from known constraints and data. However, the sensitivity tests [Figs. 3(g) and 3(h) and supplementary material S8] indicate that the shape reconstructions remain stable with respect to these parameters, and the subsequent MB pointwise reconstruction further reinforces this stability.

Real-time dose monitoring during RT is an unmet need. RAI has the potential to enable this capability. By monitoring internal organ motion using the same ultrasound (US) system employed for RAI sensing, US-derived dose maps can be co-registered to assess deviations from the treatment plan, which is typically generated from static CT images. Such a feedback allows for adaptive plan modifications and improved outcomes. Clinical implementation of RAI has been hindered by limited-view artifacts arising from restricted detector placement around the patient, and the proposed SOMB techniques directly address this. Implementing this technique will provide more reliable dose monitoring at depth, better addressing clinical needs for *in vivo* monitoring. This study currently demonstrates 2D reconstructions in uniform water phantoms and uses a single delivered beam. Its efficacy remains to be tested over the complete treatment plan multibeam delivery on complex phantoms and in humans, where internal organ motion and inherent tissue heterogeneity could affect the outcomes. Mathematically, 2D–3D transition is

30 October 2026 20:07:56

Published under an exclusive license by AIP Publishing

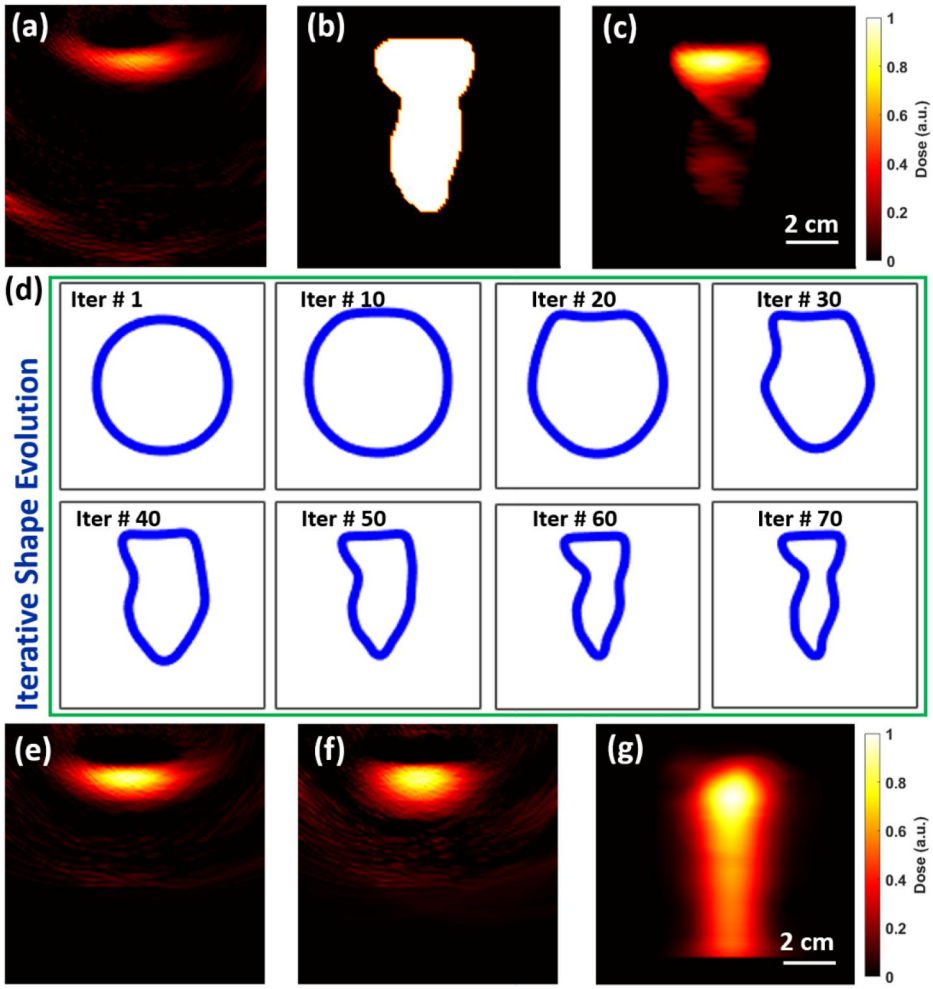

FIG. 5. Proton RAI (107.66 MeV) experimental study result. (a) The standard MB reconstruction (CC = 0.35), (b) the shape reconstruction obtained from algorithm 1, and (c) the MB RAI reconstruction evaluation in the reduced ROI (CC = 0.59). (d) The evolution of the reconstructed shape using algorithm 1 across iterations. (e) TV-MB (CC = 0.42), (f) Bregman-TV-MB (CC = 0.50), and (g) PINN reconstructions (CC = 0.86) [ROI: $10 \times 10\ \text{cm}^2$].

TABLE I. Algorithms and corresponding CC and computation time for experimental proton RAI.

Algorithm	MB	SOMB	TV	Breg+TV	PINN
CC	0.36	0.59	0.42	0.50	0.86
Time (s)	0.03	3.03	1.3	7.8	3.8

straightforward, but the computational burden grows. To keep reconstruction times compatible with clinical workflows, graphics processing unit (GPU) acceleration will be necessary.

To conclude, in the proposed RAI reconstruction methodology, the shape reconstruction of the source using the regularized trust region method defines the ROI and is considered as a spatial prior for the subsequent point-wise reconstruction. Even though the intermediate shape-reconstruction step is time consuming, it eliminates the limited-view artifacts and improves the accuracy and stability of point-wise reconstruction. Across the *in silico* and experimental RAI studies, the reconstructions thus obtained were found to be of superior quality as compared to their typical MB counterparts. The future work will focus on extending the proposed methodology to 3D and accelerating it using GPUs to enable real-time and accurate dose monitoring during RT using RAI.

See the supplementary material for detailed descriptions of the shape representation framework and the optimization algorithm used in this work. S1 describes the shape representation using RBFs, including the mollified Heaviside function and the compactly supported C^2 polynomial RBF formulation. S2–S4 provide video animations demonstrating the effect of each RBF parameter—weight (α), dilation (ζ), and center position (χ)—on the resulting level set function. S5 illustrates how four RBFs combine through superposition to form a composite shape boundary. S6 presents the trust region-based iteratively regularized quasi-Newton BFGS routine for shape reconstruction, including the full gradient derivation and sensitivity expressions. S7 provides the pseudocode for both the shape reconstruction algorithm and the shape-optimized model-based reconstruction procedure. S8 demonstrates the robustness of the reconstruction algorithm to the choice of the initial regularization parameter τ_0 and the trust region radius Δ.

30 October 2026 20:07:56

Published under an exclusive license by AIP Publishing

This work was supported by the National Institutes of Health (Nos. R37CA240806, U01CA288351, and R50CA283816). The authors would like to acknowledge the support from the UCI Chao Family Comprehensive Cancer Center (No. P30CA062203).

AUTHOR DECLARATIONS

Conflict of Interest

Liangzhong Xiang has financial interest in SoundDose, Inc., which, however, did not support this work. The remaining authors declare no conflict of interest.

Author Contributions

Prabodh Kumar Pandey: Conceptualization (lead); Data curation (lead); Formal analysis (lead); Funding acquisition (supporting); Investigation (equal); Methodology (equal); Software (equal); Supervision (equal); Writing – original draft (lead); Writing – review & editing (lead). **Omprakash Gottam:** Conceptualization (supporting); Data curation (equal); Formal analysis (supporting); Investigation (equal); Methodology (equal); Writing – original draft (supporting); Writing – review & editing (supporting). **Kristina Bjegovic:** Data curation (supporting); Investigation (supporting); Methodology (supporting). **Gilberto Gonzalez:** Data curation (supporting); Investigation (supporting); Methodology (supporting). **Yong Chen:** Funding acquisition (equal); Investigation (equal); Methodology (supporting); Resources (equal); Supervision (supporting). **Liangzhong Xiang:** Conceptualization (supporting); Funding acquisition (lead); Investigation (supporting); Methodology (supporting); Resources (lead); Supervision (equal); Writing – original draft (supporting); Writing – review & editing (supporting).

DATA AVAILABILITY

The data that support the findings of this study are available from the corresponding authors upon reasonable request.

REFERENCES

[1]Y. Xu and S. L. Xiang, "Radiacoustic imaging," Nat. Rev. Phys. **7**, 660 (2025).
[2]L. Xiang, B. Han, C. Carpenter, G. Pratx, Y. Kuang, and L. Xing, "X-ray acoustic computed tomography with pulsed x-ray beam from a medical linear accelerator," Med. Phys. **40**, 010701 (2013).
[3]L. Xiang, S. Tang, M. Ahmad, and L. Xing, "High resolution x-ray-induced acoustic tomography," Sci. Rep. **6**, 26118 (2016).
[4]S. Tang, K. Yang, Y. Chen, and L. Xiang, "X-ray-induced acoustic computed tomography for 3D breast imaging: A simulation study," Med. Phys. **45**, 1662–1672 (2018).
[5]D. Lee, E.-Y. Park, S. Choi, H. Kim, J.-j. Min, C. Lee, and C. Kim, "GPU-accelerated 3D volumetric x-ray-induced acoustic computed tomography," Biomed. Opt. Express **11**, 752–761 (2020).
[6]Y. Li, P. Samant, S. Wang, A. Behrooz, D. Li, and L. Xiang, "3-D x-ray-induced acoustic computed tomography with a spherical array: A simulation study on bone imaging," IEEE Trans. Ultrason. Ferroelectr. Freq. Control **67**, 1613–1619 (2020).
[7]E. Robertson, P. Samant, S. Wang, T. Tran, X. Ji, and L. Xiang, "X-ray-induced acoustic computed tomography (XACT): Initial experiment on bone sample," IEEE Trans. Ultrason. Ferroelectr. Freq. Control **68**, 1073–1080 (2021).
[8]P. K. Pandey, S. Wang, H. O. Aggrawal, K. Bjegovic, S. Boucher, and L. Xiang, "Model-based x-ray induced acoustic computed tomography," IEEE Trans. Ultrason. Ferroelectr. Freq. Control **68**, 3560 (2021).
[9]P. K. Pandey, S. Wang, and L. Xiang, "Model based reconstruction algorithm for x-ray induced acoustic tomography," Proc. SPIE **11595**, 115953V (2021).
[10]P. K. Pandey, G. Gonzalez, K. Bjegovic, L. Sun, Y. Chen, and L. Xiang, "3d protoacoustic radiography: A proof of principle study," Appl. Phys. Lett. **126**, 074102 (2025).
[11]S. Wang, P. K. Pandey, G. Lee, R. J. van Bergen, L. Sun, Y. Xu, and L. Xiang, "X-ray–induced acoustic computed tomography: 3D x-ray absorption imaging from a single view," Sci. Adv. **10**, eads1584 (2024).
[12]S. Hickling, M. Hobson, and I. El Naqa, "Feasibility of x-ray acoustic computed tomography as a tool for noninvasive volumetric in vivo dosimetry," Int. J. Radiat. Oncol. Biol. Phys. **90**, S843 (2014).
[13]S. Hickling, H. Lei, M. Hobson, P. Léger, X. Wang, and I. El Naqa, "Experimental evaluation of x-ray acoustic computed tomography for radiotherapy dosimetry applications," Med. Phys. **44**, 608–617 (2017).
[14]S. Hickling, M. Hobson, and I. El Naqa, "Characterization of x-ray acoustic computed tomography for applications in radiotherapy dosimetry," IEEE Trans. Radiat. Plasma Med. Sci. **2**, 337–344 (2018).
[15]J. Kim, E.-Y. Park, Y. Jung, B. C. Kim, J. H. Kim, C.-Y. Yi, I. J. Kim, and C. Kim, "X-ray acoustic-based dosimetry using a focused ultrasound transducer and a medical linear accelerator," IEEE Trans. Radiat. Plasma Med. Sci. **1**, 534–540 (2017).
[16]H. Lei, W. Zhang, I. Oraiqat, Z. Liu, J. Ni, X. Wang, and I. E. Naqa, "Toward *in vivo* dosimetry in external beam radiotherapy using x-ray acoustic computed tomography: A soft-tissue phantom study validation," Med. Phys. **45**, 4191–4200 (2018).
[17]C. H. Kim, I. J. Kim, B. C. Kim, E. Y. Park, C. Y. YI, J. Kim, J. Yuhan, J. H. Kim *et al.*, "Water dosimetry device using x-ray induced ultrasonic waves," US Patent App. 16/488,236 (2019).
[18]I. Oraiqat, W. Zhang, D. Litzenberg, K. Lam, N. Ba Sunbul, J. Moran, K. Cuneo, P. Carson, X. Wang, and I. El Naqa, "An ionizing radiation acoustic imaging (IRAI) technique for real-time dosimetric measurements for flash radiotherapy," Med. Phys. **47**, 5090–5101 (2020).
[19]S. Wang, G. Gonzalez, L. Sun, Y. Xu, P. Pandey, Y. Chen, and S. Xiang, "Real-time tracking of the bragg peak during proton therapy via 3D protoacoustic imaging in a clinical scenario," npj Imaging **2**, 34 (2024).
[20]W. Zhang, I. Oraiqat, D. Litzenberg, K.-W. Chang, S. Hadley, N. B. Sunbul, M. M. Matuszak, C. J. Tichacek, E. G. Moros, P. L. Carson *et al.*, "Real-time, volumetric imaging of radiation dose delivery deep into the liver during cancer treatment," Nat. Biotechnol. **41**, 1160–1167 (2023).
[21]Y. Huang, L. Wei, D. Litzenberg, B. Li, C. Ma, H. Kim, Y. Liu, C. Zhang, P. L. Carson, I. E. Naqa *et al.*, "Towards quantitative ionizing radiation acoustic imaging (IRAI) for radiation dose measurement: Validation from simulations to experiments," Med. Phys. **52**, e18091 (2025).
[22]K. Bjegovic, L. Sun, P. Pandey, V. Grilj, P. Ballesteros-Zebadua, R. Paisley, G. Gonzalez, S. Wang, M. C. Vozenin, C. L. Limoli *et al.*, "4D *in vivo* dosimetry for a flash electron beam using radiation-induced acoustic imaging," Phys. Med. Biol. **69**, 115053 (2024).
[23]G. T. Herman, *Fundamentals of Computerized Tomography: Image Reconstruction from Projections* (Springer Science & Business Media, 2009).
[24]U. Schneider, E. Pedroni, and A. Lomax, "The calibration of ct hounsfield units for radiotherapy treatment planning," Phys. Med. Biol. **41**, 111 (1996).
[25]G. C. Pereira, M. Traughber, and R. F. Muzic, Jr., "The role of imaging in radiation therapy planning: Past, present, and future," Biomed. Res. Int. **2014**, 231090.
[26]S. J. Gardner, J. Kim, and I. J. Chetty, "Modern radiation therapy planning and delivery," Hematol./Oncol. Clin. **33**, 947–962 (2019).
[27]L. Sun, G. Gonzalez, P. K. Pandey, S. Wang, K. Kim, C. Limoli, Y. Chen, and L. Xiang, "Towards quantitative in vivo dosimetry using x-ray acoustic computed tomography," Med. Phys. **50**, 6894–6907 (2023).
[28]G. Gonzalez, K. Prather, P. K. Pandey, L. Sun, J. Caron, S. Wang, S. Ahmad, L. Xiang, and Y. Chen, "Single-pulse x-ray acoustic computed tomographic imaging for precision radiation therapy," Adv. Radiat. Oncol. **8**, 101239 (2023).
[29]W. Assmann, S. Kellnberger, S. Reinhardt, S. Lehrack, A. Edlich, P. Thirolf, M. Moser, G. Dollinger, M. Omar, V. Ntziachristos *et al.*, "Ionoacoustic characterization of the proton bragg peak with submillimeter accuracy," Med. Phys. **42**, 567–574 (2015).
[30]J. Schauer, H.-P. Wieser, Y. Huang, H. Ruser, J. Lascaud, M. Würl, A. Chmyrov, M. Vidal, J. Herault, V. Ntziachristos *et al.*, "Proton beam range

30 October 2026 20:07:56

Published under an exclusive license by AIP Publishing

verification by means of ionoacoustic measurements at clinically relevant doses using a correlation-based evaluation," Front. Oncol. **12**, 925542 (2022).
[31]F. Forghani, A. Mahl, T. J. Patton, B. L. Jones, M. A. Borden, D. C. Westerly, C. Altunbas, M. Miften, and D. H. Thomas, "Simulation of x-ray-induced acoustic imaging for absolute dosimetry: Accuracy of image reconstruction methods," Med. Phys. **47**, 1280–1290 (2020).
[32]P. K. Pandey, S. Wang, L. Sun, L. Xing, and L. Xiang, "Model-based 3-D x-ray induced acoustic computerized tomography," IEEE Trans. Radiat. Plasma Med. Sci. **7**, 532–543 (2023).
[33]F. Natterer, "Photo-acoustic inversion in convex domains," Inverse Probl. Imaging **6**, 315–320 (2012).
[34]G. Bal and G. Uhlmann, "Inverse diffusion theory of photoacoustics," Inverse Probl. **26**, 085010 (2010).
[35]M. Haltmeier, O. Scherzer, P. Burgholzer, and G. Paltauf, "Thermoacoustic computed tomography with large planar receivers," Inverse Probl. **20**, 1663–1673 (2004).
[36]M. Xu and L. V. Wang, "Photoacoustic imaging in biomedicine," Rev. Sci. Instrum. **77**, 041101 (2006).
[37]P. Beard, "Biomedical photoacoustic imaging," Interface Focus **1**, 602–631 (2011).
[38]L. V. Wang and J. Yao, "A practical guide to photoacoustic tomography in the life sciences," Nat. Methods **13**, 627–638 (2016).
[39]F. Santosa, "A level-set approach for inverse problems involving obstacles fadil santosa," ESAIM: COCV. **1**, 17–33 (1996).
[40]A. D. Zacharopoulos, S. R. Arridge, O. Dorn, V. Kolehmainen, and J. Sikora, "Three-dimensional reconstruction of shape and piecewise constant region values for optical tomography using spherical harmonic parametrization and a boundary element method," Inverse Probl. **22**, 1509 (2006).
[41]N. Naik, J. Eriksson, P. de Groen, and H. Sahli, "A nonlinear iterative reconstruction and analysis approach to shape-based approximate electromagnetic tomography," IEEE Trans. Geosci. Remote Sens. **46**, 1558–1574 (2008).
[42]A. Aghasi, M. Kilmer, and E. L. Miller, "Parametric level set methods for inverse problems," SIAM J. Imag. Sci. **4**, 618–650 (2011).
[43]N. Naik, N. Patil, Y. Yadav, J. Eriksson, and A. Pradhan, "Fully nonlinear sp_3 approximation based fluorescence optical tomography," IEEE Trans. Med. Imaging **36**, 2308–2318 (2017).
[44]O. Gottam, N. Naik, and S. Gambhir, "Parameterized level-set based pharmacokinetic fluorescence optical tomography using the regularized gauss–newton filter," J. Biomed. Opt. **24**, 1–031010 (2018).
[45]O. Gottam, N. Naik, P. Kumar Pandey, and S. Gambhir, "Rbf level-set based fully-nonlinear fluorescence photoacoustic pharmacokinetic tomography," Inverse Probl. Sci. Eng. **29**, 3227–3260 (2021).
[46]H. Wendland, *Scattered Data Approximation* (Cambridge University Press, 2004), Vol. 17.
[47]T. Bonnafont and F. Caubet, "A robust inverse scattering method based on shape optimization," in *IEEE Conference on Antenna Measurements and Applications (CAMA)* (IEEE, 2023), pp. 1–6.
[48]L. Audibert, H. Haddar, and X. Liu, "An accelerated level-set method for inverse scattering problems," SIAM J. Imag. Sci. **15**, 1576–1600 (2022).
[49]M. Xu and L. V. Wang, "Universal back-projection algorithm for photoacoustic computed tomography," Phys. Rev. E **71**, 016706 (2005).
[50]L. V. Wang and H.-i. Wu, *Biomedical Optics: Principles and Imaging* (John Wiley & Sons, 2012).
[51]T. F. Chan and L. A. Vese, "Active contours without edges," IEEE Trans. Image Process. **10**, 266–277 (2001).
[52]K. C. Jones, C. M. Seghal, and S. Avery, "How proton pulse characteristics influence protoacoustic determination of proton-beam range: Simulation studies," Phys. Med. Biol. **61**, 2213 (2016).
[53]X. L. Deán-Ben and D. Razansky, "On the link between the speckle free nature of optoacoustics and visibility of structures in limited-view tomography," Photoacoustics **4**, 133–140 (2016).
[54]X. L. Deán-Ben, L. Ding, and D. Razansky, "Dynamic particle enhancement in limited-view optoacoustic tomography," Opt. Lett. **42**, 827–830 (2017).
[55]J. Zhu, N. Huynh, O. Ogunlade, R. Ansari, F. Lucka, B. Cox, and P. Beard, "Mitigating the limited view problem in photoacoustic tomography for a planar detection geometry by regularized iterative reconstruction," IEEE Trans. Med. Imaging **42**, 2603–2615 (2023).
[56]S. Gazzola, P. C. Hansen, and J. G. Nagy, "IR tools: A MATLAB package of iterative regularization methods and large-scale test problems," Numer. Algorithms **81**, 773–811 (2019).
[57]L. Sun, K. Bjegovic, L. Rodriguez-Gonzalez, Y. Xu, Y. Yan, G. Gonzalez, L. Whitmore, L. Connell, Y. Lang, P. Pandey *et al.*, "A physics-informed neural network for *in vivo* dosimetry using quantitative radiacoustic imaging," Res. Sq. 3.rs-8503498 (2026).

30 October 2026 20:07:56

Published under an exclusive license by AIP Publishing